Published in final edited form as:
Metallomics. 2013 November ; 5(11): 1554–1565. doi:10.1039/c3mt00133d.

X-ray Fluorescence Imaging of the Hippocampal Formation After Manganese Exposure†

Gregory Robison[a], **Taisiya Zakharova**[a], **Sherleen Fu**[b], **Wendy Jiang**[b], **Rachael Fulper**[a], **Raul Barrea**[c,d], **Wei Zheng**[b], and **Yulia Pushkar**[a,*]

[a]Purdue University, Department of Physics, 525 Northwestern Avenue, West Lafayette, IN 47907, USA

[b]Purdue University, School of Health Sciences, 550 Stadium Mall Drive, West Lafayette, IN 47907, USA

[c]DePaul University, Department of Physics, 2219 North Kenmore Avenue Suite 211, Chicago, IL 60614, USA

[d]Argonne National Laboratory, Advanced Photon Source, 9700 South Cass Avenue, Argonne, IL 60437, USA (former affiliation)

Abstract

Manganese (Mn) intoxication results in neurological conditions similar, but not identical, to idiopathic Parkinson's disease. While the mechanism(s) by which Mn exposure leads to neurotoxic effects remains unclear, studies by magnetic resonance imaging demonstrate a high Mn accumulation in the hippocampal formation (HPCf) of the brain. Metal quantification using this method is not possible. Using x-ray fluorescence imaging, we measured the distribution of Mn in the HPCf for a rodent model of chronic Mn exposure and quantitatively compared it with distributions of other biologically relevant metals. We found considerable increases in average Mn concentrations in all analyzed areas and we identified the dentate gyrus (DG) and the cornus ammonis 3 (CA3) layer as areas accumulating the highest Mn content (~1.2 μg Mn/g tissue). The DG is significantly enriched with iron (Fe), while the CA3 layer has high zinc (Zn) content. Additionally, significant spatial correlations were found for Mn/Zn concentrations across the identified substructures of the HPCf and for Mn/Fe concentrations in the DG. Combined results support that at least two mechanisms may be responsible for Mn transport and/or storage in the brain, associated with either Fe or Zn. Subcellular resolution images of metal distribution in cells of the CA3 show diffuse Mn distributions consistent with Mn localization in both the cytoplasm and nucleus. Mn was not increased in localized intracellular Fe or copper accumulations. A consistent Mn/Zn correlation both at the tissue (40 μm × 40 μm) and cellular (0.3 μm × 0.3 μm) levels suggests that a Zn transport/storage mechanism in the HPCf is likely associated with Mn accumulation.

†Electronic Supplementary Information (ESI) available: Glial fibrillary acidic protein immunohistochemistry protocol and method used for determining the minimum detection and analyzable limites. Fig. S1 HPCf cell scan locations; Fig. S2 HPCf CA3 Control cells; Fig. S3 HPCf CA3 Mn treated cells; HPCf 1-5 pixel scatter plots; Fig. S5 Pixel scatter plots of CA3 cells; Fig. S6 Glial fibrillary acidic protein immunohistochemical staining of the HPCf; Table S1 Minimum detection and analzable limits; Table S2 Linear fit parameters for HPCf pixel scatter plots. See DOI: 10.1039/b000000x/

Fax: (765)494-0706; Tel: (765)496-3276, ypushkar@purdue.edu.

Introduction

Trace metals serve an important role in proper development and function of the brain. Under physiological conditions manganese (Mn) serves as a cofactor to various proteins including phosphoenolpyruvate carboxykinase[1–2], mitochondrial superoxide dismutase[3], glutamine-synthetase[4–6], pyruvate carboxylase[7–8], and arginase[9]. The disruption of trace metal homeostasis has been linked to a wide variety of neurological disorders; overexposure to Mn results in a neurological condition known as *manganism*, first reported by Couper[10]. Populations at risk include miners, smelters, and welders, professions where the airborne Mn concentrations are high[11–25]; patients suffering from cirrhosis of the liver , which is responsible for removal of Mn from the blood[26–32]; and those who use methcathinone (or ephendrone), an illegal substance produced using potassium permanganate[33–35]. Symptoms of *manganism* include tremor, bradykinesia, impaired postural reflexes, dystonia, gait problems, memory loss, apathy, and psychosis, several of these symptoms are also exemplified in Parkinson's disease[17,29,36–38]. Unlike those suffering from Parkinson's disease, patients with *manganism* do not respond to L-dopa therapy[39–40].

Despite being described over 170 years ago, the molecular mechanism(s) resulting in *manganism* are not well understood. Magnetic resonance imaging (MRI) has provided novel insights; Mn^{2+} is paramagnetic and therefore Mn exposure results in enhanced contrast of the T_1 relaxation time. Increased signal intensity in T_1-weighted MRI has been observed in the globus pallidus (GP) of occupationally exposed workers[25, 41–45] as well as in substantia nigra reticulate[35]. Additionally, MRI has been used to study the kinetics of Mn uptake in rodent models[46–50]. Using this method, it has been shown that Mn enters the cerebral spinal fluid via the choroid plexus in less than 10 minutes following injection, spreading to the sub-structures of the hippocampal formation (HPCf) such as the cornu ammonis 3 (CA3) in 4–24 hours[47–48, 50]. MRI generally demonstrates Mn accumulation in the HPCf in rodents exposed to Mn but not in the GP and/or the substantia nigra[51], in contrast to other techniques such as atomic absorption spectroscopy (AAS)[52], inductively coupled plasma mass spectroscopy[53], and x-ray fluorescence (XRF) imaging[54]. This discrepancy has not been resolved, although it has been suggested that the Mn binding environment or speciation can critically affect its MRI T_1 relaxation properties[55–57].

XRF imaging provides a unique tool for studying metal distribution *in situ* under the condition of Mn intoxication. Unlike MRI, XRF imaging can simultaneously measure the concentration and distribution of multiple metals in a single scan, regardless of binding environment[49, 54, 58–65] and has previously been used to study the distribution of metals within the HPCf[49,61–63,66]. Furthermore, XRF is regularly performed at resolutions on the order of microns at a 'typical' synchrotron facility beamline or down to 30 nanometers at specialized beamlines. Previously we reported quantitative XRF analysis of Mn distribution in thin tissue brain sections from a rodent model of Mn intoxication, demonstrating accumulation in the GP, thalamus, and substantia nigra compact[54]. While Mn accumulation in the basal ganglia is likely responsible for motor dysfunction, Mn accumulation in HPCf might be related to mood stability, memory loss, and learning disorders[67–68]. Using XRF imaging and cluster analysis we studied Mn, iron (Fe), copper (Cu) and zinc (Zn) content in the HPCf in a rat model of chronic Mn exposure. XRF imaging allowed us to uncover a strong correlation between Mn and Zn distributions in HPCf. We also report the first single cell XRF imaging of Mn in brain slices, showing a diffuse Mn distribution in CA3 cells.

Experimental Procedures

Animal treatment

Animal selection and treatment closely follow those described in [69]. Briefly, 8 week old Sprague-Dawley rats (Harlan, Indianapolis) were randomly divided into two groups ($n = 4$ per group) and were housed in a temperature controlled, 12/12 hour light/dark room. Not all animals were used for a given imaging experiment. Animals were allowed free access to de-ionized water and food (Purina rodent chow 5001, 70 ppm Mn content). At the beginning of the 9th week, animals received intraperitoneal (i.p.) injections of either 6 mg Mn/kg body weight in solution (treated group) or an equal volume of saline solution (control group). Injections were performed on weekdays for a period of four weeks and rats sacrificed 24 hours after the last injection. Plasma Mn concentrations for control and treated animals following this protocol have been reported to be 3.5 ± 0.3 μg/L and 34.8 ± 2.3 μg/L respectively, measured at 24 hours after the last injection[69]. Following sacrifice, brains were removed from the skull, blotted to remove excess blood from the exterior of the structure, and snap frozen in liquid nitrogen. Samples were stored at −80 °C. Twelve hours prior to sectioning brains were transferred to a −20 °C freezer; this ensures optimal sample temperature and prevents cracking of the sample during sectioning. All experiments complied with animal rights regulations and were approved by the Institutional Committee on Animal Use at Purdue University.

Preparation of brain sections

Thin tissue brain sections were obtained using a Shandon Cryotome; a frozen sample was attached to a cryocassette at the cerebellum using Tissue-Teck O.C.T. Compound (metal free) and mounted to the cryotome cutting head. The cutting chamber temperature was maintained at −12 °C during the cutting process. Tissue sections (10 μm and 30 μm thick) were thawed on 4 μm thick polypropylene film secured to plastic frames; 10 μm thick sections were also collected on glass slides (for immunohistochemistry). Bregma locations of −2.64 mm and −5.20 mm were chosen as they displayed the HPCf, as well as other brain structures of interest for a different study. Locations were confirmed by cresyl violet staining of adjunct sections and visual identification of structures. Once placed on the substrate, sections were covered and returned to −80 °C for storage. To avoid modification of metal distribution chemical fixation was not applied to the brain tissue.

Synchrotron based XRF

XRF imaging was performed at the Advanced Photon Source (APS); large area scans (~mm^2) of coronal sections were taken at Sector 18, the Biophysics Collaborative Access Team (BioCAT) facilities[70–71] and single cell imaging (~100 μm^2) was performed at Sector 2-ID-D[72]. Unless otherwise noted, 30 μm thick sections were used for XRF imaging; samples were removed from dry ice, mounted to the beamline, and imaged at room temperature in air (BioCAT measurements) or in helium (Sector 2-ID-D measurements). Samples generally air dry within 2 minutes of removal from dry ice. Spectra were collected on a pixel by pixel basis at a 10 keV incident energy and the MAPS program[73] was used for fitting. Thin film standards (NBS-1832/33) allow for metal quantification. Table 1 lists the XRF imaging parameters used for this study and Table S1 lists the minimum detection and analyzable limits for the respective data collections. Data collected at BioCAT had the low Z element contributions to the spectrum suppressed by placing two, 8 μm aluminium filters over the detector collimator affording a larger collection solid angle while preventing detector saturation. The detector to sample distance was determined by optimizing the ratio of signal to total counts of the unfitted Mn K_α peak thereby minimizing the background contribution to the spectrum. Single cell measurements taken at Sector 2-ID-D were performed in a helium bag to record the low Z element contributions to the spectrum.

Cluster Analysis

The HPCf was visually identified and its extent delineated by hand taking care to avoid the central and lateral ventricles adjacent to the structure. As the substructures of the HPCf are heterogeneous in metal content[49,62,66,74], *k*-means cluster analysis was employed to objectively identify separate regions. Clustering used both the Fe and Zn signals at equal weights; Fe alone failed to identify the CA3 whereas Zn alone did not delineate the dentate gyrus (DG). Contaminants and/or bubbles would result in a small cluster (<10 pixels) being identified; such pixels were deselected and the analysis repeated. Blood vessels were identified by their strong Fe content as compared to surrounding tissue and their circular shape; vessels were removed before analysis. Five clusters were chosen as more clusters did not delineate any additional, unique anatomical structures. As many as 8 clusters were used on any sample that failed to identify clusters consistent with other samples; in this event, clusters were then merged to form the five clusters. Statistical significance between groups was determined by one-way analysis of variance (ANOVA); analysis of covariance (ANCOVA) was used to determine the similarity of linear regression where appropriate. All statistical analysis used $\alpha = 0.05$ unless otherwise noted.

Cell body identification

Potassium (K) co-localized with both sulphur (S) and phosphorus (P), indicating that the sample drying did not result in leaching from the cell (Fig 4). Therefore, delineation of the cell was performed using the potassium (K) signal which presented good contrast between the cell body and the surrounding space. Specifically, an exponential filter was applied for contrast enhancement, followed by convolution with a 10 pixel median filter to despeckle the region. The dynamic range of the image was then compressed to 8-bit grayscale and an unsharp mask applied for edge detection. The largest continuous region was then taken to be the cell body.

Results

HPCf substructure delineation by cluster analysis

Coronal sections of the rodent brain displaying the HPCf were XRF imaged at 10 keV to obtain Mn, Fe, Cu, and Zn distributions. Comparison with thin film standards allowed for metal quantification. The HPCf is comprised of multiple substructures which demonstrate varying degrees of metal accumulation; Fig. 1A presents a diagram of the HPCf with distinct anatomical regions labeled. To delineate these regions in an objective manner, *k*-means cluster analysis was performed, resulting in identification of the main anatomical substructures (Fig. 1B). Substructures were grouped as follows: green (HPCf 1) stratum oriens (So) and stratum raditum (Sr); blue (HPCf 2) entorhinal cortex (EC), hippocampal fissure (hf), and molecular layer of the DG (MoDG); cyan (HPCf 3) CA3; magenta (HPCf 4) DG and CA1; yellow (HPCf 5) the polymorphic layer of the DG (PoDG). Fig. 1C shows the distribution patterns of Mn, Fe, Cu and Zn in HPCf of control and treated animals. Mn accumulation is readily seen in the CA2–3 and DG regions of treated samples but is still noticeable in the control section (different intensity scale maximum). Fe was most notably contained within the granular cell layer of the DG and the CA1 whereas Zn was primarily located in the PoDG and the CA3–4. Cu was located along the hf and the upper portion of the So. The circular areas of Fe content predominantly observed in the hf are blood vessels (Fig. 1C); these areas were excluded prior to analysis. Using the aforementioned clustering, average metal concentration of the regions was calculated and compared. This study found statistically significant Mn increase in treated animals across five identified HPCf regions as compared to control (Table 2). The only other statistically significant change in concentration was a 27% decrease in the Fe content of the HPCf 4 in the Mn treated group as compared to control.

Manganese correlation with other metals

Two color maps of Mn/Fe, Mn/Cu, and Mn/Zn showed that Mn co-localizes with Zn in the CA3 and to a lesser extent with Fe in the DG (Fig. 2A). To further examine Mn co-localization with biologically significant metal ions, scatter plots of the average metal concentration (Fe, Cu, or Zn) in regions identified by cluster analysis versus Mn concentrations were created and fitted with a linear regression weighted by data point variance (Fig. 2B). For treated samples a strong, positive correlation between Zn and Mn ($r = 0.68$, $p < 0.01$) and a weaker, negative correlation between Cu and Mn ($r = -0.52$, $p = 0.01$) were observed. The correlation between Fe and Mn was not statistically significant ($r = -0.33$, $p = 0.14$). For control samples, the Cu/Mn and Zn/Mn correlations were not statistically significant ($r = 0.39$, $p = 0.27$ and $r = -0.06$, $p = 0.87$ respectively), but a strong correlation was observed in Fe/Mn ($r = 0.87$, $p < 0.01$). Curiously, correlations seen in one sample group are anti-correlated in the other. Table 3 summarized the fit parameters and correlation results.

The DG, where our analysis showed co-localization of the Fe and Mn signals (Fig. 2A), was quite small and thus a scan of the crest of the DG was performed in treated rat at increased pixel resolution (7 μm × 7 μm; Fig. 3A). This scan clearly showed Mn accumulation in the blades of the DG which was 17% higher than the Mn concentration in the immediate surrounding area. Fe was also concentrated in this area, although it appeared to be contained within a narrower region. The mean metal concentrations and linear fit parameters are presented in Table 2 and Table 4, respectively. Scatter plots of pixel metal concentrations demonstrated that Mn moderately correlated with Fe ($r = 0.35$, $p < 0.01$) within the DG. Cu did not correlate with Mn in any of the regions examined. Small 'hotspots' of high Cu concentration were observed within the PoDG which were not visible at lower resolution (40 μm × 40 μm). These hotspots are likely the result of Cu accumulations in astrocytes[80]. The PoDG region was rich in Zn but did not show a significant correlation with Mn ($r = -0.01$, $p = 0.77$). The strongest correlation was observed between Mn and Zn in HPCf2 (blue; $r = 0.51$, $p < 0.01$).

Subcellular XRF imaging of Mn

Cells of the CA3 were selected for single cell imaging due to the high Mn concentration in this area and the ease by which the CA3 is identified by its strong Zn content (Fig. S1). Measured cells were likely neurons which demonstrate Zn accumulation within synaptic vesicles[62,81]. The majority of single cell measurements were performed on 30 μm thick tissue sections to ensure sufficient statistics for fitting; imaging thinner sections was prohibitively long for the available amount of beamtime. Pyramidal cells of the CA3 layer have been reported to be between 17.6 – 31 μm in diameter (soma area between 246 – 750 μm^2)[82] and therefore, assuming a pyramidal cell has been selected, less than two full cells should be present through the depth of the sample. A total of 11 control and 9 treated cells were measured ($n = 4/3$ control/treated; Figs. 4, S3, & S4). We do not think that sample drying resulted in significant redistribution of elements. For instance, if such re-distribution would occur, K would be the first element to re-distribute due to its high mobility. However, K co-localizes with both S and P (Fig. 4), elements that are bound to bio-molecules and therefore do not easily diffuse. Thus, K did not leach from the cell due to sample drying and therefore re-distribution of other elements is similarly insignificant. Sample thickness obscured the nucleus/cell body boundary and therefore subcellular divisions were not considered. Nevertheless, localized Fe and Cu hotspots are easily visible; should highly localized Mn accumulations occur they should similarly be detectable. Cellular trace metal concentrations (Table 5) were higher as compared to the images of the bulk structures (*i.e.* 40 μm × 40 μm pixel size). This is likely due to heterogeneous distribution of metal inside and outside the cells. Chronic Mn exposure resulted in the significant increase of Mn content

inside cells. Differences in average elemental content (P, S, K, Cl, Ca, K, Fe, Cu, & Zn) between the control and treated cells were not statistically significant (Table 5 & Fig. S5). The large standard deviations demonstrated a high degree of cell-to-cell variability in intracellular metal contents (Fig. S5A). Potassium is distributed throughout the soma and therefore can be used to delineate the extent of the cell body. From visual inspection, Mn is distributed throughout the cell, although high Mn concentration appears in the areas of high P and K content. The Fe distribution is highly heterogeneous inside the cells with small, localized accumulations that do not co-localize with any other element. Cu hotspots, on the order of microns in size, appeared at the extremities of the cell body; these are likely occurred inside astrocytes or their processes which propagated between the measured cells[80](Fig. S6).

Due to the cell-to-cell variation in metal content, additional data processing was performed to produce pixel scatter plots. For a given cell, the average metal content was subtracted from each pixel value. Data were then binned and plotted as a 2-dimensional histogram (Fig. S5B); linear regression parameters of un-binned data are reported (Table 6). For both control and treated cells, the strongest correlations observed are between Mn/K for both control and treated cells followed by Mn/Zn. Both Mn/K and Mn/Zn have a 60% decrease in scatter plot slope in treated samples which is statistically significant according to ANCOVA.

In comparison with cells of the subventricular zone (SVZ) processed in a similar fashion (data not shown), the P and K content were on the same order of magnitude whereas dramatic differences were seen in Fe, Cu, and Zn contents. Astrocytes of the SVZ are known to accumulate unusually high Cu on the order of 100 mM concentrations[80]. Thus, the average Cu concentration of CA3 cells was 20–30 times lower than that demonstrated for SVZ cells. The average Fe content was a factor of four lower in CA3 cells than SVZ cells; the reason for this difference is unclear. Zn was approximately 60% higher in the CA3 cells likely due to Zn storage in synaptic vesicles. Comparison of Mn content was not possible as SVZ cells were not imaged with sufficient dwell time for proper Mn counting statistics.

Discussion

Mn accumulation and distribution in the hippocampus has been studied previously by MRI[47–50,83–84], radiography[85], and XRF[49]. From a survey of literature, it is clear that the amount of Mn retained in HPCf depends on the Mn administration protocol and time between last Mn injection and animal sacrifice. Thus, Mn accumulation and retention in HPCf is presumably a highly dynamic process.

Qualitatively, Mn distribution in the hippocampus has been monitored by increased MRI T_1 weighted signal intensity for both acute[47–50] and chronic Mn exposure[83]. The strongest signal enhancements were noted in the CA3 and DG with the weakest being in the CA1[47–48]. Similar enhancement of the CA3 and DG has been noted for neonatal (P4) mice 24 hours post injection[84]. In agreement with previous studies[47–50], our data highlight the CA3 and DG as targets of Mn accumulation in condition of chronic Mn exposure; the PoDG, identified due to increased resolution, can also be included.

Quantitatively, considering the HPCf as a single unit, the average Mn content measured in this study is only 30% higher than reported in[75] where quantification was performed by AAS. Both studies used the same animal treatment protocol, however, for our study the post-injection time was only 24 hours rather than 2 weeks. Using neutron activation analysis (NAA), Moldovan, Al-Ebraheem, Miksys, Farquharson and Bock[77] reported a Mn content twice as large as this study for the same absolute Mn exposure (120 mg Mn total), however treatment was over a period of 4 days resulting in a higher daily dose. This shows that

capacity of the HPCf in accommodating Mn was not saturated in our study. A study using a single dose of 30 mg Mn/kg[49] measured Mn concentrations 2–3 times higher than this study. Fe values given in [77] and [75] are up to 2 times higher than reported here; Cu concentrations are 3.25 times higher. For Fe, this discrepancy is due mainly to the precision of tissue sampling; the specified studies dissected the hippocampal region without removal of the blood vessels whereas the current study excluded all nearby blood vessels. It is known that brain capillaries accumulate Fe, in both free and transferrin-bound forms, 108 times more than the capillary-depleted parenchyma[86]. Hence, the increased Fe in hippocampus observed in the previous study could be contributed by Fe accumulation in hippocampal capillary. Similarly, inadequate separation of the HPCf from the SVZ could result in the inclusion of high Cu accumulations which could skew Cu measurements to higher concentrations. Daoust, Barbier and Bohic[49] noted decreased Fe content in the HPCf as a result of Mn exposure, in agreement with this study, although decreased Fe or Zn (Table 2) were generally not significant.

Whether considering the HPCf as a single structure or as the 5 identified regions, Mn concentrations in control samples were comparable to those of the cortex and the G[54]. Thus, at the normal condition HPCf does not contain more Mn than other major brain structures. For treated samples, Mn content in the HPCf3–5 (1.21 ± 0.22, 1.26 ± 0.13, and 1.21 ± 0.08 μg/g respectively) was approximately equivalent to concentrations measured in the substantia nigra compacta (1.21 ± 0.17 μg/g), thalamus (1.15 ± 0.12 μg/g), and the GP (1.53 ± 0.10 μg/g)[54]; suggesting that the HPCf3–5 are equivalently susceptible to Mn insult.

The effect of Mn on Fe homeostasis has been implicated as one possible mechanism of Mn induced neurotoxicity[69,87]. Transferrin receptor mediated endocytosis has been proposed to transport Mn into the cell in the form of Mn^{3+}-transferrin complex[88]. It has been shown that Fe deficiency results in the up-regulation of transferrin and transferrin receptor expression[89–90], and that dietary Mn exposure coupled with Fe deficiency results in an increased Mn uptake into the HPCf[90–92]. Our earlier studies of other brain areas also had shown positive correlation between Fe content and Mn accumulation[54]. Mn accumulation in the DG, the area of highest Fe content, suggests that Fe transport may play a role in Mn uptake in this structure. Furthermore, Fe content in this region was observed to decrease significantly, possibly suggesting either competition between Fe and Mn for transport or a saturation of transport into/storage within the cell. The slope of Mn/Fe scatter plot of HPCf regions changes from positive to negative between control and treated brain (Fig. 2B) also suggesting the saturation of Fe pathway for Mn transport in the HPCf. Visualization at single cell resolution presents a picture with defined Fe accumulation inside cells of the CA3 which do not show Mn co-accumulation and are not altered with Mn exposure. Mn distribution inside cell is diffuse whereas Fe is found in small concentrated regions (Fig. 4). Thus, intracellular Fe and Mn are bound/localized differently.

The moderate Mn/Cu anti-correlation supports that sites of Cu accumulation do not correspond to areas of high Mn content. Cu has been shown to accumulate in astrocytes, both in culture[93–95] and in brain tissue[80]. It is therefore plausible that Cu hotspots may indicate, in part, astrocyte location. Astrocytes are thought to be one target of Mn accumulation as the glia-specific enzyme glutamine synthetase[96–97] can bind to as many as 8 Mn atoms per octamer[5], accounting for roughly 80% of Mn in the healthy brain[4]. Under normal physiological conditions, only 30% of glutamine synthetase is saturated with Mn, providing capacity for cellular storage. Indeed, Mn has been observed to accumulate in the hf, an area of the HPCf rich in astrocytes, as a result of an acute intracerebral injection[49]; i.p. injections used in the aforementioned study or our study do not demonstrate a similar accumulation. Immunohistochemical staining of glial fibrillary acidic protein, a marker of astrocytes, demonstrated the most intense expression in the hf where the lowest

concentrations of Mn were observed (Fig. S6). The lack of any correlation between Mn and Cu provides further evidence that astrocytes are not the primary target of Mn accumulation in this rodent model in agreement with previous studies[49,54].

The strong Mn/Zn correlation (Fig. 2, Table 3) between regions identified by cluster analysis suggests a rapport between the transport and/or accumulation of Mn and Zn in HPCf under condition of Mn intoxication (note that correlations are weaker in control samples). It appears to be unique to HPCf since analysis of other brain structures shown only moderate correlation for group of selected brain structures (see Figure 5 in [54]). Two separate families of proteins serve opposing functions for Zn transport in cells; the Zrt- Irt-like protein (ZIP) family serves for cellular Zn influx while the Zn transporter family (ZnT) transports Zn within and out of the cell[98–100]. The ZIP8 protein is responsible for Zn^{2+} transport across the cell membrane but has also been established as a cadmium transporter. A competitive inhibition between cadmium and manganese has been observed in cell cultures[101–103] and cadmium resistant cells have shown a similar resistance to Mn accumulation[103]. Lastly, ZIP8 is a symporter of bicarbonate which could explain increased Mn concentrations with increasing extracellular pH levels[103–105]. A ZIP8 hypomorph model[106] could be of use for future investigations with regards to Mn intoxication. In HPCf the Zn transporter 3 (ZnT3) is expressed in hippocampal mossy fibers as identified by Timm's staining[81], suggesting that ZnT3 is responsible for Zn accumulation in synaptic vesicles[107]. A transgenic mice model with ZnT3 knockout has shown decreased Zn in the HPCf highlighting the role of ZnT3[62,81,108]. Zn ions are released during synaptic transmission, however, their exact physiological role(s) remain unknown. A recent study[109] reporting a decrease in spatial memory additionally suggests depletion of Zn in the HPCf may play a role in memory and behaviour. This is in contrast to Cole, et al.[110] which supports that spatial learning is not impaired in this rodent model. As Mn distribution shows strong correlation with Zn, one can propose that Mn in HPCf is stored in synaptic vesicles and released during synaptic transmission; presumably interfering with Zn homeostasis, altering synaptic transmission and, thus, contributing to neurological disturbances.

Conflicting reports in literature discuss the preferential targets of Mn location inside the intoxicated cells mainly focusing on mitochondria, the nucleus or the Golgi apparatus[58,111–112]. Due to mobile nature of the Mn^{2+} ion in the brain tissue, significant care must be taken for sample preparation. Perfusion of the brain results in approximately a 50% decrease in Mn content[111] and any chemical treatment of brain tissue depletes majority of Mn^{2+} from the samples[54]. Accordingly, unperfused, chemically untreated samples must be used for imaging of Mn distributions. To the best of our knowledge there is only one imaging study of Mn distribution in cells (PC12 cells culture) prepared by cryofixation[58]. Cell cultures are quite different from brain cells *in situ* as the brain barriers that regulate trace metal access are absent. The strongest correlation observed in our single cell study is for Mn/K (Table 6). Our results agree with Ayotte and Plaa[113] which reports comparable Mn concentration in the cytoplasm and nucleus up to 3 hours post-injection. However, considering both the sample thickness used for this study and the sample variability observed Fig. S5), additional work is necessary to examine subcellular accumulation *in situ* using XRF imaging. Clearly no localized Mn accumulations were observed in examined cells.

Conclusion

Here we present the quantitative imaging analysis of the effects of chronic Mn exposure on metal accumulation within the HPCf as measured by XRF. Statistically significant increases in Mn concentration were observed for all substructures of the HPCf as well as a decreased Fe concentration in the DG ($p < 0.01$). Manganese was confirmed to preferentially

accumulate in the DG, PoDG, and CA3 (~1.2 μg/g); this concentration is less than that observed for the GP (~1.5 μg/g) but roughly that of the substantia nigra and thalamus (~1.2 μg/g)[54]. A strong Mn/Zn positive correlation ($r = 0.68$, $p < 0.01$) was found across the five divisions of the HPCf. We suggest that this could be indicative of a global Zn associated mechanism for Mn transport and/or storage within the HPCf, with potential involvements of specifically ZIP8 or ZnT3 (transporter primarily found in mossy fibers of the HPCf). The changed Mn/Fe scatter plot slope for treated samples as compared to control is possibly due to a saturation of a Fe transport/storage mechanism; presumably this mechanism is more strongly expressed in the DG thereby explaining the statistically significant decrease in Fe concentration. Further study is necessary to solidify this inference.

Single cell imaging of CA3 neurons revealed an increased Mn concentration, however cell to cell variability prevents any other meaningful statement regarding other elements. Cellular distribution of Mn was diffuse, confirmed by a strong correlation in with K (control and treated, $r > 0.50$, $p < 0.01$) which is known to be present throughout the nucleus and cytoplasm. The areas of higher Mn accumulation do not co-localize with the small, of high Fe or Cu concentrations ($r < 0.15$).

Supplementary Material

Refer to Web version on PubMed Central for supplementary material.

Acknowledgments

We thank Dr. Barry Lai for his assistance in operating Sector 2-ID-D beamline and Dr. Stefan Vogt for his help in using the MAPS program. Use of the Advanced Photon Source, an Office of Science User Facility operated for the U.S. Department of Energy (DOE) Office of Science by Argonne National Laboratory, was supported by the U.S. DOE under Contract No. DE-AC02-06CH11357. BioCAT is a National Institutes of Health-supported Research Center RR-08630. This study was supported by NIH/National Institute of Environmental Health Sciences Grants Numbers R01 ES008146-14, and by Purdue startup funds.

Abbreviation

ANCOVA	Analysis of covariance
ANOVA	Analysis of variance
APS	Advanced Photon Source
AAS	Atomic absorption spectroscopy
BioCAT	Biophysics Collaborative Access Team
CA1–4	Cornus ammonis 1–4
DG	Dentate gyrus
EC	Entorhinal cortex
GP	Globus pallidus
hf	Hippocampal fissure
HPCf	Hippocampal formation
i.p.	Intraperitoneal
MRI	Magnetic resonance imaging
MoDG	Molecular layer of the dentate gyrus

NAA	Neutron activation analysis
PoDG	Polymorphic layer of the dentate gyrus
So	Stratum oriens
Sr	Stratum raditum
SVZ	Sub-ventricular zone
XRF	X-ray fluorescence
ZnT	Zinc transporter family
ZIP	Zrt- Irt-like protein

Notes and references

1. Baly DL, Keen CL, Hurley LS. Pyruvate-Carboxylase and Phosphoenolpyruvate Carboxykinase Activity in Developing Rats - Effects of Manganese Deficiency. J. Nutr. 1985; 115:872–879. [PubMed: 4009297]
2. Nowak, T. Manganese in Metabolism and Enzyme Function. Schramm, VL.; Wedler, FC., editors. Academic Press Inc.; 1986. p. 165-191.
3. Akai F, Maeda M, Suzuki K, Inagaki S, Takagi H, Taniguchi N. Immunocytochemical localization of manganese superoxide-dismutase (Mn-SOD) in the hippocampus of the rat. Neurosci. Lett. 1990; 115:19–23. [PubMed: 2216054]
4. Wedler FC, Denman RB. Glutamin-synthetase - the majory Mn(II) enzyme in mammalian brain. Curr. Top. Cell. Regul. 1984; 24:153–169. [PubMed: 6149889]
5. Wedler FC, Denman RB, Roby WG. Glutamine-synthetase from ovine brain is a manganese(II) enzyme. Biochemistry. 1982; 21:6389–6396. [PubMed: 6129892]
6. Pinkofsky HB, Maurizi MR, Ginsburg A. Binding Mn2+ or Mg2+ to active sites of glutamine-synthetase from bovine brain. Fed. Proc. 1985; 44:1807–1807.
7. Mildvan AS, Scrutton MC. Pyruvate Carboxylase. X. The Demonstration of Direct Coordination of Pyruvate and α-Ketobutyrate by the Bound Manganese and the Formation of Enzyme-Metal-Substrate Bridge Complexes*. Biochemistry. 1967; 6:2978–2994. [PubMed: 6069856]
8. Scrutton, MC. Manganese in Metabolism and Enzyme Function. Schramm, VL.; Wedler, FC., editors. Academic Press Inc.; 1986. p. 147-163.
9. Reczkowski RS, Ash DE. EPR evidence for binuclear manganese(II) centers in rat liver arginase. J. Am. Chem. Soc. 1992; 114:10992–10994.
10. Couper J. On the effects of black oxide of manganese which inhaled inot the lungs. Brit. Ann. Med. Pharmacol. 1837; 1:41–42.
11. Rybicki BA, Johnson CC, Uman J, Gorell JM. Parkinsons disease mortality and the intdustrial use of heavy metals in Michigan. Mov. Disord. 1993; 8:87–92. [PubMed: 8419812]
12. Gorell JM, Johnson CC, Rybicki BA, Peterson EL, Kortsha GX, Brown GG, Richardson RJ. Occupational exposures to metals as risk factors for Parkinson's disease. Neurology. 1997; 48:650–658. [PubMed: 9065542]
13. Lucchini RG, Albini E, Benedetti L, Borghesi S, Coccaglio R, Malara EC, Parrinello G, Garattini S, Resola S, Alessio L. High prevalence of parkinsonian disorders associated to manganese exposure in the vicinities of ferroalloy industries. Am. J. Ind. Med. 2007; 50:788–800. [PubMed: 17918215]
14. Bouchard M, Mergler D, Baldwin ME, Panisset M. Manganese cumulative exposure and symptoms: A follow-up study of alloy workers. Neurotoxicology. 2008; 29:577–583. [PubMed: 18562007]
15. Huang CC, Chu NS, Lu CS, Chen RS, Schulzer M, Calne DB. The natural history of neurological manganism over 18 years. Parkinsonism Relat. Disord. 2007; 13:143–145. [PubMed: 17052946]

16. Huang CC, Chu NS, Lu CS, Chen RS, Calne DB. Long-term progression in chronic manganism - Ten years of follow-up. Neurology. 1998; 50:698–700. [PubMed: 9521259]

17. Cersosimo MG, Koller WC. The diagnosis of manganese-induced parkinsonism. Neurotoxicology. 2006; 27:340–346. [PubMed: 16325915]

18. Sadek AH, Rauch R, Schulz PE. Parkinsonism due to Manganism in a Welder. Int. J. Toxicol. 2003; 22:393–401. [PubMed: 14555414]

19. Marsh GM, Gula MJ. Employment as a welder and Parkinson disease among heavy equipment manufacturing workers. J. Occup. Environ. Med. 2006; 48:1031–1046. [PubMed: 17033503]

20. Cowan DM, Zheng W, Zou Y, Shi XJ, Chen J, Rosenthal FS, Fan QY. Manganese exposure among smelting workers: Relationship between blood manganese-iron ratio and early onset neurobehavioral alterations. Neurotoxicology. 2009; 30:1214–1222. [PubMed: 19963104]

21. Gorell JM, Peterson EL, Rybicki BA, Johnson CC. Multiple risk factors for Parkinson's disease. J. Neurol. Sci. 2004; 217:169–174. [PubMed: 14706220]

22. Firestone JA, Lundin JI, Powers KM, Smith-Weller T, Franklin GM, Swanson PD, Longstreth WT, Checkoway H. Occupational Factors and Risk of Parkinson's Disease: A Population-Based Case-Control Study. Am. J. Ind. Med. 2010; 53:217–223. [PubMed: 20025075]

23. Racette BA, Tabbal SD, Jennings D, Good L, Perlmutter JS, Evanoff B. Prevalence of parkinsonism and relationship to exposure in a large sample of Alabama welders. Neurology. 2005; 64:230–235. [PubMed: 15668418]

24. Li GJJ, Zhang LL, Lu L, Wu P, Zheng W. Occupational exposure to welding fume among welders: Alterations of manganese, iron, zinc, copper, and lead in body fluids and the oxidative stress status. J. Occup. Environ. Med. 2004; 46:241–248. [PubMed: 15091287]

25. Jiang YM, Zheng W, Long LL, Zhao WJ, Li XR, Mo XA, Lu JP, Fu X, Li WM, Liu ST, Long QY, Huang JL, Pira E. Brain magnetic resonance imaging and manganese concentrations in red blood cells of smelting workers: Search for biomarkers of manganese exposure. Neurotoxicology. 2007; 28:126–135. [PubMed: 16978697]

26. Barron TF, Devenyi AG, Mamourian AC. Symptomatic Manganese Neurotoxicity in a Patient with Chronic Liver-Disease = Correlation of Clinical Symptoms with MRI Findings. Pediatr. Neurol. 1994; 10:145–148. [PubMed: 8024663]

27. Devenyi AG, Barron TF, Mamourian AC. Dystonia, Hyperintense Basal Ganglia, and High Whole-Blood Manganese Leves in Alagilles Syndrome. Gastroenterology. 1994; 106:1068–1071. [PubMed: 8143974]

28. Hauser RA, Zesiewicz TA, Rosemurgy AS, Martinez C, Olanow CW. Manganese Intoxication and Chronic Liver-Failure. Ann. Neurol. 1994; 36:871–875. [PubMed: 7998773]

29. Klos KJ, Ahlskog JE, Josephs DA, Fealey RD, Cowl CT, Kumar N. Neurologic spectrum of chronic liver failure and basal ganglia T1 hyperintensity on magnetic resonance imaging - Probable manganese neurotoxicity. Arch. Neurol. 2005; 62:1385–1390. [PubMed: 16157745]

30. Krieger D, Krieger S, Jansen O, Gass P, Theilmann L, Lichtnecker H. Manganese and Chronic Heptatic-Encephalopathy. Lancet. 1995; 346:270–274. [PubMed: 7630246]

31. Burkhard PR, Delavelle J, Du Pasquier R, Spahr L. Chronic Parkinsonism associated with cirrhosis - A distinct subset of acquired hepatocerebral degeneration. Arch. Neurol. 2003; 60:521–528. [PubMed: 12707065]

32. Long LL, Li XR, Huang ZK, Jiang YM, Fu SX, Zheng W. Relationship Between Changes in Brain MRI and H-1-MRS, Severity of Chronic Liver Damage, and Recovery After Liver Transplantation. Exp. Biol. Med. 2009; 234:1075–1085.

33. Stepens A, Logina I, Liguts V, Aldins P, Eksteina I, Platkajis A, Martinsone I, Terauds E, Rozentale B, Donaghy M. A Parkinsonian syndrome in methcathinone users and the role of manganese. N. Engl. J. Med. 2008; 358:1009–1017. [PubMed: 18322282]

34. Meral H, Kutukcu Y, Atmaca B, Ozer F, Hamamcioglu K. Parkinsonism caused by chronic usage of intravenous potassium permanganate. Neurologist. 2007; 13:92–94. [PubMed: 17351530]

35. Levin OS. "Ephedron" encephalopathy. Zhurnal Nevrologii I Psikhiatrii Imeni S S Korsakova. 2005; 105:12–20. [PubMed: 16117141]

36. Crossgrove J, Zheng W. Manganese toxicity upon overexposure. NMR Biomed. 2004; 17:544–553. [PubMed: 15617053]

37. Aschner M, Guilarte TR, Schneider JS, Zheng W. Manganese: Recent advances in understanding its transport and neurotoxicity. Toxicol. Appl. Pharmacol. 2007; 221:131–147. [PubMed: 17466353]
38. Josephs KA, Ahlskog JE, Klos KJ, Kumar N, Fealey RD, Trenerry MR, Cowl CT. Neurologic manifestations in welders with pallidal MRI T1 hyperintensity. Neurology. 2005; 64:2033–2039. [PubMed: 15888601]
39. Koller WC, Lyons KE, Truly W. Effect of levodopa treatment for parkinsonism in welders - A double-blind study. Neurology. 2004; 62:730–733. [PubMed: 15007122]
40. Guilarte TR. Manganese and Parkinson's Disease: A Critical Review and New Findings. Environ. Health Perspect. 2010; 118:1071–1080. [PubMed: 20403794]
41. Dietz MC, Ihrig A, Wrazidlo W, Bader M, Jansen O, Triebig G. Results of magnetic resonance imaging in long-term manganese dioxide-exposed workers. Environ. Res. 2001; 85:37–40. [PubMed: 11161650]
42. Kim Y, Kim KS, Yang JS, Park IJ, Kim E, Jin YW, Kwon KR, Chang KH, Kim JW, Park SH, Lim HS, Cheong HK, Shin YC, Park J, Moon Y. Increase in signal intensities on T1-weighted magnetic resonance images in asymptomatic manganese-exposed workers. Neurotoxicology. 1999; 20:901–907. [PubMed: 10693971]
43. Nelson K, Golnick J, Korn T, Angle C. Manganese encephalopathy - utility of early magnetic-resonance-imaging. Br. J. Ind. Med. 1993; 50:510–513. [PubMed: 8329316]
44. Lucchini R, Albini E, Placidi D, Gasparotti R, Pigozzi MG, Montani G, Alessio L. Brain magnetic resonance imaging and manganese exposure. Neurotoxicology. 2000; 21:769–775. [PubMed: 11130281]
45. Dydak U, Jiang YM, Long LL, Zhu H, Chen JA, Li WM, Edden RAE, Hu SG, Fu X, Long ZY, Mo XA, Meier D, Harezlak J, Aschner M, Murdoch JB, Zheng W. In Vivo Measurement of Brain GABA Concentrations by Magnetic Resonance Spectroscopy in Smelters Occupationally Exposed to Manganese. Environ. Health Perspect. 2011; 119:219–224. [PubMed: 20876035]
46. London RE, Toney G, Gabel SA, Funk A. Magnetic resonance imaging studies of the brains of anesthetized rats treated with manganese chloride. Brain Res. Bull. 1989; 23:229–235. [PubMed: 2819480]
47. Aoki I, Wu YJL, Silva AC, Lynch RM, Koretsky AP. In vivo detection of neuroarchitecture in the rodent brain using manganese-enhanced MRI. Neuroimage. 2004; 22:1046–1059. [PubMed: 15219577]
48. Watanabe T, Natt O, Boretius S, Frahm J, Michaelis T. In vivo 3D MRI staining of mouse brain after subcutaneous application of MnCl2. Magn. Reson. Med. 2002; 48:852–859. [PubMed: 12418000]
49. Daoust A, Barbier EL, Bohic S. Manganese enhanced MRI in rat hippocampus: A correlative study with synchrotron X-ray microprobe. NeuroImage. 2013; 64:10–18. [PubMed: 22995778]
50. Lee JH, Silva AC, Merkle H, Koretsky AP. Manganese-enhanced magnetic resonance imaging of mouse brain after systemic administration of MnCl2: Dose-dependent and temporal evolution of T-1 contrast. Magn. Reson. Med. 2005; 53:640–648. [PubMed: 15723400]
51. Mok SI, Munasinghe JP, Young WS. Infusion-based manganese-enhanced MRI: a new imaging technique to visualize the mouse brain. Brain. Struct. Funct. 2012; 217:107–114. [PubMed: 21597966]
52. Bonilla E. Flameless atomic absorption spectrophotometric determination of manganese in rat brain and other tissues. Clin. Chem. 1978; 24:471–474. [PubMed: 630709]
53. Tarohda T, Ishida Y, Kawai K, Yamamoto M, Amano R. Regional distributions of manganese, iron, copper, and zinc in the brains of 6-hydroxydopamine-induced parkinsonian rats. Anal. Bioanal. Chem. 2005; 383:224–234. [PubMed: 16132122]
54. Robison G, Zakharova T, Fu S, Jiang W, Fulper R, Barrea R, Marcus MA, Zheng W, Pushkar Y. X-Ray Fluorescence Imaging: A New Tool for Studying Manganese Neurotoxicity. PLoS One. 2012; 7:e48899. [PubMed: 23185282]
55. Kang YS, Gore JC, Armitage IM. Studies of factors affecting the design of NMR contrast agents - Manganese in blood as a model system. Magn. Reson. Med. 1984; 1:396–409. [PubMed: 6443783]

56. Drahoš B, Lukeš I, Tóth É. Manganese(II) Complexes as Potential Contrast Agents for MRI. Eur. J. Inorg. Chem. 2012; 2012:1975–1986.
57. Koylu MZ, Asubay S, Yilmaz A. Determination of Proton Relaxivities of Mn(II), Cu(II) and CRIII) added to Solutions of Serum Proteins. Molecules. 2009; 14:1537–1545. [PubMed: 19384283]
58. Carmona A, Deves G, Roudeau S, Cloetens P, Bohic S, Ortega R. Manganese Accumulates within Golgi Apparatus in Dopaminergic Cells as Revealed by Synchrotron X-ray Fluorescence Nanoimaging. ACS Chem. Neurosci. 2010; 1:194–203. [PubMed: 22778823]
59. Popescu BFG, George MJ, Bergmann U, Garachtchenko AV, Kelly ME, McCrea RPE, Luning K, Devon RM, George GN, Hanson AD, Harder SM, Chapman LD, Pickering IJ, Nichol H. Mapping metals in Parkinson's and normal brain using rapid-scanning x-ray fluorescence. Phys. Med. Biol. 2009; 54:651–663. [PubMed: 19131671]
60. Yoshida S, Ektessabi A, Fujisawa S. XANES spectroscopy of a single neuron from a patient with Parkinson's disease. J. Synchrotron Radiat. 2001; 8:998–1000. [PubMed: 11513007]
61. Miller LM, Wang Q, Telivala TP, Smith RJ, Lanzirotti A, Miklossy J. Synchrotron-based infrared and X-ray imaging shows focalized accumulation of Cu and Zn co-localized with beta-amyloid deposits in Alzheimer's disease. J. Struct. Biol. 2006; 155:30–37. [PubMed: 16325427]
62. Linkous DH, Flinn JM, Koh JY, Lanzirotti A, Bertsch PM, Jones BF, Giblin LJ, Frederickson CJ. Evidence that the ZNT3 protein controls the total amount of elemental zinc in synaptic vesicles. J. Histochem. Cytochem. 2008; 56:3–6. [PubMed: 17712179]
63. Gu H, Robison G, Hong L, Barrea R, Wei X, Farlow MR, Pushkar YN, Du Y, Zheng W. Increased β-amyloid deposition in Tg-SWDI transgenic mouse brain following in vivo lead exposure. Toxicol. Lett. 2012; 213:211–219. [PubMed: 22796588]
64. Kosior E, Bohic S, Suhonen H, Ortega R, Deves G, Carmona A, Marchi F, Guillet JF, Cloetens P. Combined use of hard X-ray phase contrast imaging and X-ray fluorescence microscopy for sub-cellular metal quantification. J. Struct. Biol. 2012; 177:239–247. [PubMed: 22182730]
65. Carmona A, Cloetens P, Deves G, Bohic S, Ortega R. Nano-imaging of trace metals by synchrotron X-ray fluorescence into dopaminergic single cells and neurite-like processes. J. Anal. At. Spectrom. 2008; 23:1083–1088.
66. Leskovjan AC, Kretlow A, Lanzirotti A, Barrea R, Vogt S, Miller LM. Increased brain iron coincides with early plaque formation in a mouse model of Alzheimer's disease. NeuroImage. 2011; 55:32–38. [PubMed: 21126592]
67. Wasserman GA, Liu XH, Parvez F, Ahsan H, Levy D, Factor-Litvak P, Kline J, van Geen A, Slavkovich V, Lolacono NJ, Cheng ZQ, Zheng Y, Graziano JH. Water manganese exposure and children's intellectual function in Araihazar, Bangladesh. Environ. Health Perspect. 2006; 114:124–129. [PubMed: 16393669]
68. Scoville WB, Milner B. Loss of recent memory after bilateral hippocampal lesions. J. Neurol., Neurosurg. Psychiatry. 1957; 20:11–21. [PubMed: 13406589]
69. Zheng W, Zhao QQ, Slavkovich V, Aschner M, Graziano JH. Alteration of iron homeostasis following chronic exposure to manganese in rats. Brain Res. 1999; 833:125–132. [PubMed: 10375687]
70. Barrea RA, Fischetti R, Stepanov S, Rosenbaum G, Kondrashkina E, Bunker GB, Black E, Zhang K, Gore D, Heurich R, Vukonich M, Karanfil C, Kropf AJ, Wang S, Irving TC. Biological XAFS at the BioCAT undulator beamline 18ID at the APS. Phys. Scr. 2005; T115:867–869.
71. Barrea RA, Gore D, Kujala N, Karanfil C, Kozyrenko S, Heurich R, Vukonich M, Huang R, Paunesku T, Woloschak G, Irving TC. Fast-scanning high-flux microprobe for biological X-ray fluorescence microscopy and microXAS. J. Synchrotron Radiat. 2010; 17:522–529. [PubMed: 20567085]
72. Cai, Z.; Lai, B.; Yun, W.; McNulty, I.; Khounsary, A.; Maser, J.; Ilinski, P.; Legnini, D.; Trakhtenberg, E.; Xu, S.; Tieman, B.; Wiemerslage, G.; Gluskin, E. Synchrotron Radiation Instrumentation. Pianetta, P.; Arthur, J.; Brennan, S., editors. Vol. vol. 521. 2000. p. 31-34.
73. Vogt S. MAPS: A set of software tools for analysis and visualization of 3D X-ray fluorescence data sets. J. Phys. IV. 2003; 104:635–638.

74. Becker JS. Bioimaging of metals in brain tissue from micrometre to nanometre scale by laser ablation inductively coupled plasma mass spectrometry: State of the art and perspectives. Int. J. Mass Spectrom. 2010; 289:65–75.
75. Zheng W, Jiang YM, Zhang YS, Jiang WD, Wang XQ, Cowan DM. Chelation therapy of manganese intoxication with para-aminosalicylic acid (PAS) in Sprague-Dawley rats. Neurotoxicology. 2009; 30:240–248. [PubMed: 19150464]
76. Szerdahelyi P, Kása P. Variations in trace metal levels in rat hippocampus during ontogenetic development. Anat Embryol. 1983; 167:141–149. [PubMed: 6881542]
77. Moldovan N, Al-Ebraheem A, Miksys NA, Farquharson MJ, Bock NA. Altered transition metal homeostasis in mice following manganese injections for manganese-enhanced magnetic resonance imaging. BioMetals. 2013; 26:179–187. [PubMed: 23334711]
78. Lai JCK, Minski MJ, Chan AWK, Leung TKC, Lim L. Manganese mineral interactions in brain. Neurotoxicology. 1999; 20:433–444. [PubMed: 10385902]
79. Lai JCK, Minski MJ, Chan AWK, Lim L, Davison AN. Brain regional manganese distribution after chronic manganese treatment. Biochem. Soc. Trans. 1981; 9:228.
80. Pushkar Y, Robison G, Sullivan B, Fu SX, Kohne M, Jiang W, Rohr S, Lai B, Marcus MA, Zakharova T, Zheng W. Aging results in copper accumulations in glial fibrillary acidic protein-positive cells in the subventricular zone. Aging Cell. 2013
81. Wenzel HJ, Toby BC, Born DE, Schwartzkroin PA, Palmiter RD. Ultrastructural Localization of Zinc Transporter-3 (ZnT-3) to Synaptic Vesicle Membranes within Mossy Fiber Boutons in the Hippocampus of Mouse and Monkey. Proc. Natl. Acad. Sci. U. S. A. 1997; 94:12676–12681. [PubMed: 9356509]
82. Ishizuka N, Cowan WM, Amaral DG. A quantitative analysis of the dendritic organization of pyramidal cells in the rat hippocampus. J. Comp. Neurol. 1995; 362:17–45. [PubMed: 8576427]
83. Grünecker B, Kaltwasser SF, Zappe AC, Bedenk BT, Bicker Y, Spoormaker VI, Wotjak CT, Czisch M. Regional specificity of manganese accumulation and clearance in the mouse brain: implications for manganese-enhanced MRI. NMR Biomed. 2012 n/a-n/a.
84. Wadghiri YZ, Blind JA, Duan X, Moreno C, Yu X, Joyner AL, Turnbull DH. Manganese-enhanced magnetic resonance imaging (MEMRI) of mouse brain development. NMR Biomed. 2004; 17:613–619. [PubMed: 15761950]
85. Takeda A, Akiyama T, Sawashita J, Okada S. Brain uptake of trace metals, zinc and manganese, in rats. Brain Res. 1994; 640:341–344. [PubMed: 8004463]
86. Deane R, Zheng W, Zlokovic BV. Brain capillary endothelium and choroid plexus epithelium regulate transport of transferrin-bound and free iron into the rat brain. J. Neurochem. 2004; 88:813–820. [PubMed: 14756801]
87. Garcia SJ, Gellein K, Syversen T, Aschner M. A manganese-enhanced diet alters brain metals and transporters in the developing rat. Toxicol. Sci. 2006; 92:516–525. [PubMed: 16705042]
88. Aisen P, Aasa R, Redfield AG. Chromium, manganese, and cobalt complexes of transferrin. J. Biol. Chem. 1969; 244:4628-&. [PubMed: 4309148]
89. Erikson KM, Pinero DJ, Connor JR, Beard JL. Regional brain iron, ferritin and transferrin concentrations during iron deficiency and iron repletion in developing rats. J. Nutr. 1997; 127:2030–2038. [PubMed: 9311961]
90. Chua A, Morgan E. Effects of iron deficiency and iron overload on manganese uptake and deposition in the brain and other organs of the rat. Biol. Trace Elem. Res. 1996; 55:39–54. [PubMed: 8971353]
91. Erikson KA, Shihabi ZK, Aschner JL, Aschner M. Manganese accumulates in iron-deficient rat brain regions in a heterogeneous fashion and is associated with neurochemical alterations. Biol. Trace Elem. Res. 2002; 87:143–156. [PubMed: 12117224]
92. Garcia SJ, Gellein K, Syversen T, Aschner M. Iron deficient and manganese supplemented diets alter metals and transporters in the developing rat brain. Toxicol. Sci. 2007; 95:205–214. [PubMed: 17060373]
93. Qian YC, Tiffanycastiglioni E, Harris ED. Copper transport and kinetics in cultured C6 rat glioma-cells. Am. J. Physiol.: Cell Physiol. 1995; 269:C892–C898.

94. Brown DR. Role of the prion protein in copper turnover in astrocytes. Neurobiol. Dis. 2004; 15:534–543. [PubMed: 15056461]

95. Scheiber IF, Mercer JFB, Dringen R. Copper accumulation by cultured astrocytes. Neurochem. Int. 2010; 56:451–460. [PubMed: 20004225]

96. Martinez-Hernandez A, Bell KP, Norenberg MD. Glutamine synthetase - glial localization in brain. Science. 1977; 195:1356–1358. [PubMed: 14400]

97. Norenberg MD, Martinez-Hernandez A. Fine structural localization of glutamine-synthetase in astrocytes of rat brain. Brain Res. 1979; 161:303–310. [PubMed: 31966]

98. Liuzzi JP, Cousins RJ. Mammlian Zinc Transporters. Annu. Rev. Nutr. 2004; 24:151–172. [PubMed: 15189117]

99. Eide DJ. Zinc transporters and the cellular trafficking of zinc. Biochim. Biophys. Acta, Mol. Cell Res. 2006; 1763:711–722.

100. Lichten LA, Cousins RJ. Annu. Rev. Nutr. 2009; vol. 29:153–176. [PubMed: 19400752]

101. Fujishiro H, Doi M, Enomoto S, Himeno S. High sensitivity of RBL-2H3 cells to cadmium and manganese: an implication of the role of ZIP8. Metallomics. 2011; 3:710–718. [PubMed: 21509381]

102. Rousselet E, Richaud P, Douki T, Chantegrel JG, Favier A, Bouron A, Moulis JM. A zinc-resistant human epithelial cell line is impaired in cadmium and manganese import. Toxicol. Appl. Pharmacol. 2008; 230:312–319. [PubMed: 18433815]

103. Yanagiya T, Imura N, Enomoto S, Kondo Y, Himeno S. Suppression of a high-affinity transport system for manganese in cadmium-resistant metallothionein-null cells. J. Pharmacol. Exp. Ther. 2000; 292:1080–1086. [PubMed: 10688626]

104. He L, Girijashanker K, Dalton TP, Reed J, Li H, Soleimani M, Nebert DW. ZIP8, member of the solute-carrier-39 (SLC39) metal-transporter family: Characterization of transporter properties. Mol. Pharmacol. 2006; 70:171–180. [PubMed: 16638970]

105. Martin P, Fareh M, Poggi MC, Boulukos KE, Pognonec P. Manganese is highly effective in protecting cells from cadmium intoxication. Biochem. Biophys. Res. Commun. 2006; 351:294–299. [PubMed: 17055454]

106. Wang B, He L, Dong HB, Dalton TP, Nebert DW. Generation of a Slc39a8 hypomorph mouse: Markedly decreased ZIP8 Zn(2+)/(HCO(3)(−))(2) transporter expression. Biochem. Biophys. Res. Commun. 2011; 410:289–294. [PubMed: 21658371]

107. Palmiter RD, Cole TB, Quaife CJ, Findley SD. ZnT-3, a putative transporter of zinc into synaptic vesicles. Proc. Natl. Acad. Sci. U. S. A. 1996; 93:14934–14939. [PubMed: 8962159]

108. Cole TB, Wenzel HJ, Kafer KE, Schwartzkroin PA, Palmiter RD. Elimination of zinc from synaptic vesicles in the intact mouse brain by disruption of the ZnT3 gene. Proc. Natl. Acad. Sci. U. S. A. 1999; 96:1716–1721. [PubMed: 9990090]

109. Martel G, Hevi C, Kane-Goldsmith N, Shumyatsky GP. Zinc transporter ZnT3 is involved in memory dependent on the hippocampus and perirhinal cortex. Behav. Brain Res. 2011; 223:233–238. [PubMed: 21545813]

110. Cole TB, Martyanova A, Palmiter RD. Removing zinc from synaptic vesicles does not impair spatial learning, memory, or sensorimotor functions in the mouse. Brain Res. 2001; 891:253–265. [PubMed: 11164830]

111. Morello M, Canini A, Mattioli P, Sorge RP, Alimonti A, Bocca B, Forte G, Martorana A, Bemardi G, Sancesario G. Subcellular localization of manganese in the basal ganglia of normal and manganese-treated rats - An electron spectroscopy imaging and electron energy-loss spectroscopy study. Neurotoxicology. 2008; 29:60–72. [PubMed: 17936361]

112. Kalia K, Jiang W, Zheng W. Manganese accumulates primarily in nuclei of cultured brain cells. Neurotoxicology. 2008; 29:466–470. [PubMed: 18400301]

113. Ayotte P, Plaa GL. Hepatic subcellular distribution of manganese in manganese and manganese-bilirubin induced cholestasis. Biochem. Pharmacol. 1985; 34:3857–3865. [PubMed: 4062960]

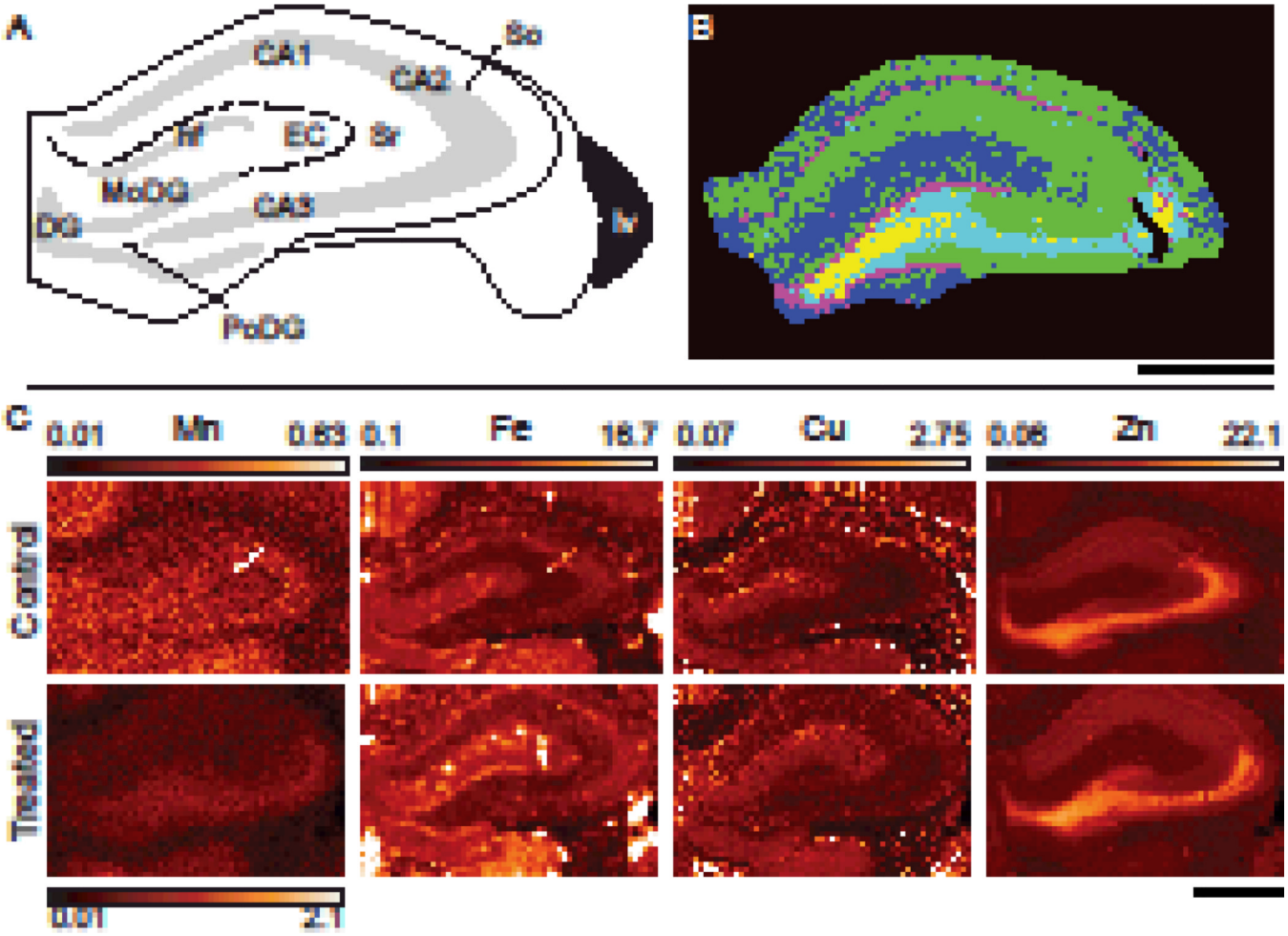

Fig. 1. XRF imaging of the hippocampal formation

(A) Diagram of the HPCf identifying the main anatomical structures present. CA1–3, cornu ammonis 1–3; DG, dentate gyrus; hf, hippocampal fissure; EC, entorhinal cortex; lv, lateral ventricle; MoDG, molecular layer of the DG; PoDG, polymorphic layer of the DG; SO, stratum oriens; SR, stratum radiatum. (B) A typical result of *k*-mean cluster analysis using the Zn and Fe signals at equal weights where the HPCf is divided into five regions; HPCf1–5 are green, blue, cyan, magenta, and yellow respectively. (C) XRF imaging of coronal sections (Bregma −2.64 mm) of control and Mn treated samples. Note that the maximum Mn concentration for control is 30% of that for the Mn treated. All numbers are given in μg/g. Scale bars represent a length of 1 mm.

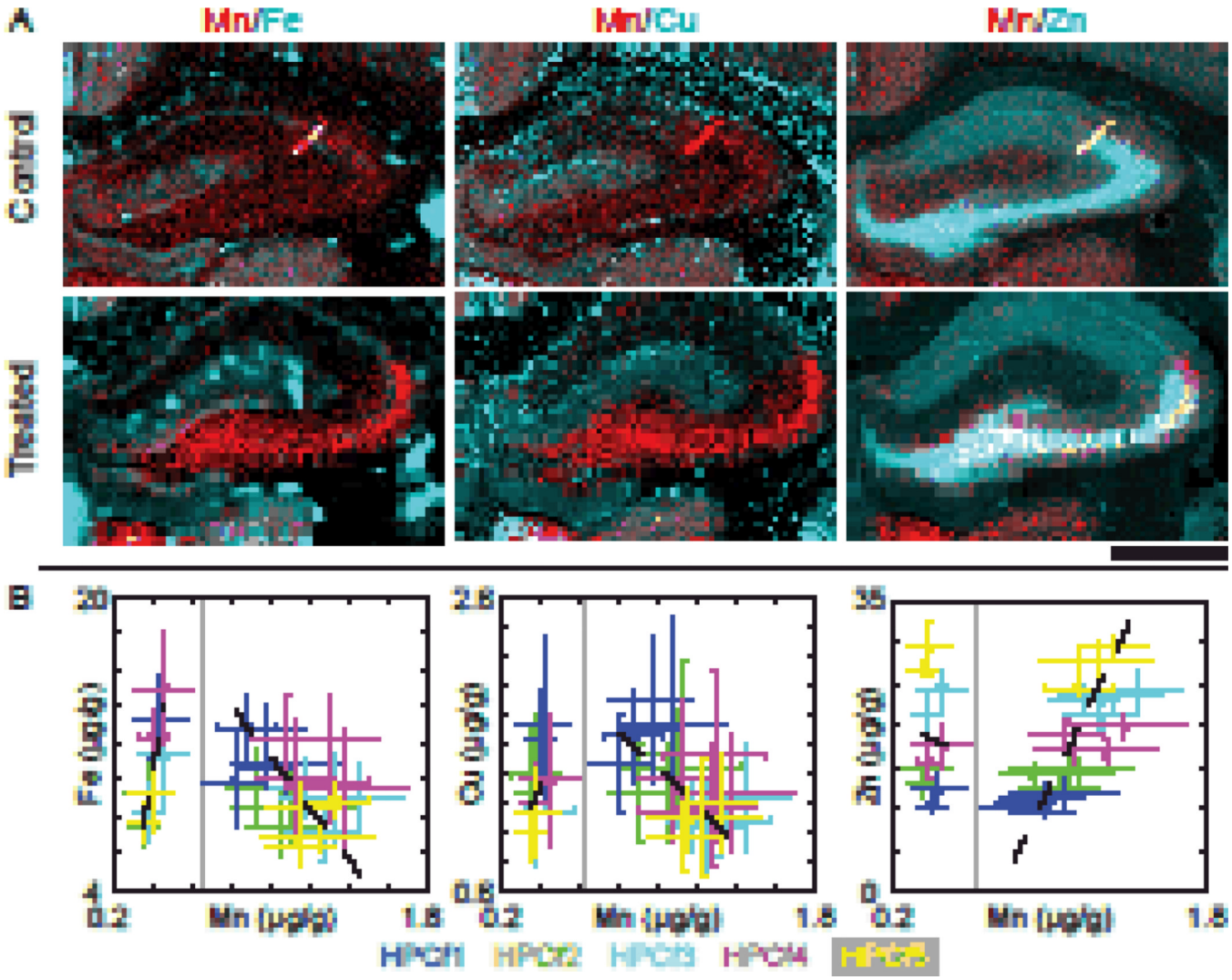

Fig. 2. Analysis of the hippocampal formation regions

(A) Two colored images displaying Fe/Mn, Cu/Mn, and Zn/Mn respectively. Note that Mn and Zn strongly co-localize in the CA3 of the HPCf, while a small portion of Mn also co-localizes with Fe within the DG as indicated by white pixels in the images. Scale bar represents a length of 1 mm. (B) Scatter plots of the mean concentrations of regions identified by clustering. Points are color-matched to the regions specified in Fig. 1B and bars indicate the standard deviation for the given data points. Data points from control/treated samples are to the left/right of the vertical grey line respectively; $n = 2/4$ animals (control/treated) for HPCf 1&2, and $n = 2/3$ for HPCf 3–5. One treated animal was measured at both Bregma locations. Linear fit parameters and respective Pearson's correlation coefficients are given in Table 3. Fits were weighted according to the variance of the data points. All numbers are given in μg/g.

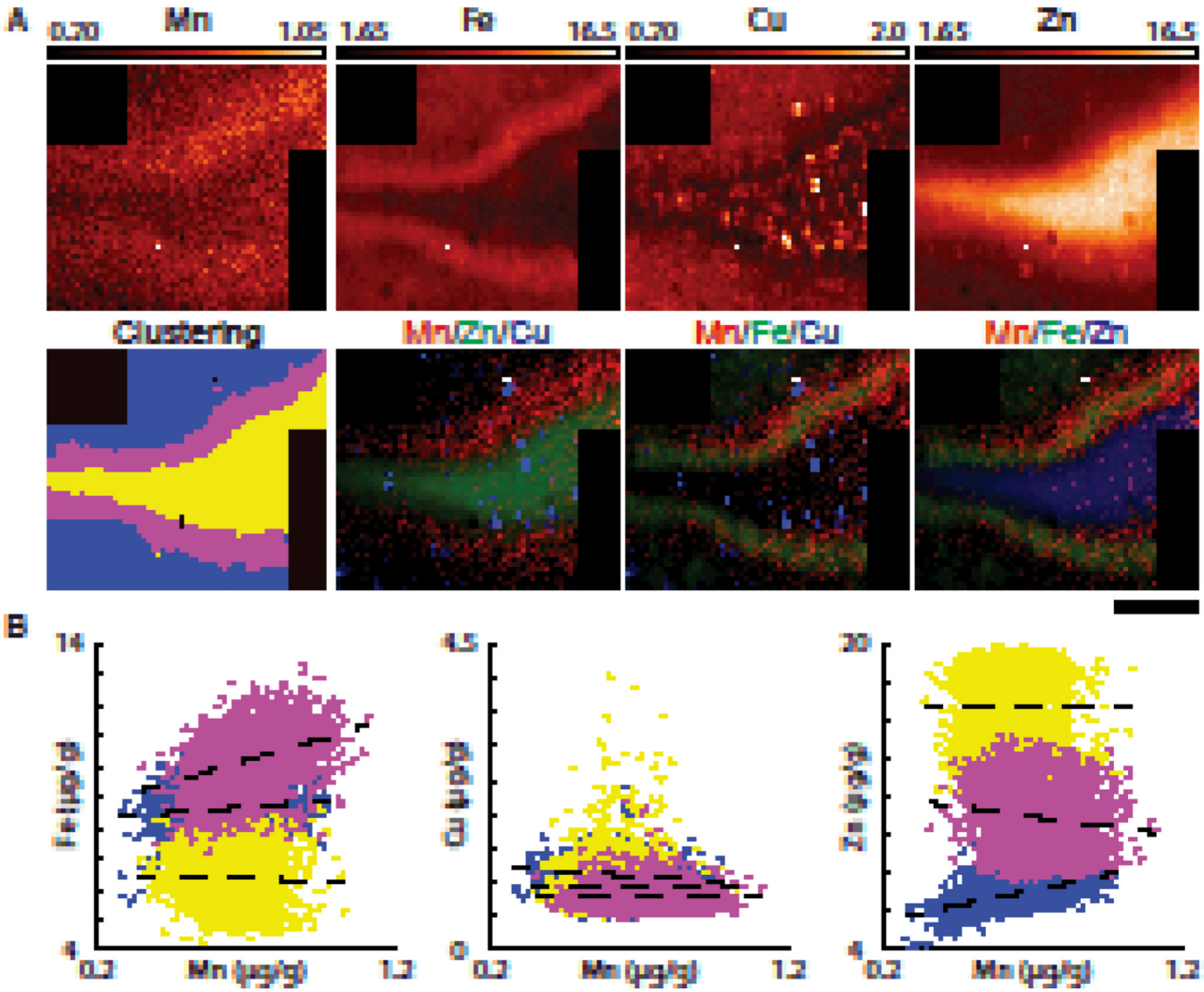

Fig. 3. XRF image of the crest of the dentate gyrus

(A) XRF image of the DG of a Mn treated sample take with 7 × 7 μm2 pixel size. Cluster analysis (k = 3) using Fe and Zn identified HPCf 2 (blue), HPCf 4 (magenta), and HPCf 5 (yellow). Tri-colored images demonstrate an accumulation of Mn in the DG which is enriched with Fe but not in the PoDG. All numbers are given in μg/g. Scale bar represents a length of 200 μm. (B) Scatter plots of pixel data from these three regions are displayed. The strongest correlations observed are Mn/Fe in HPCf4 ($r = 0.35$, $p<0.01$) and Mn/Zn in HPCf2 ($r = 0.51$, $p<0.01$). A summary of fit parameters are given in Table 4.

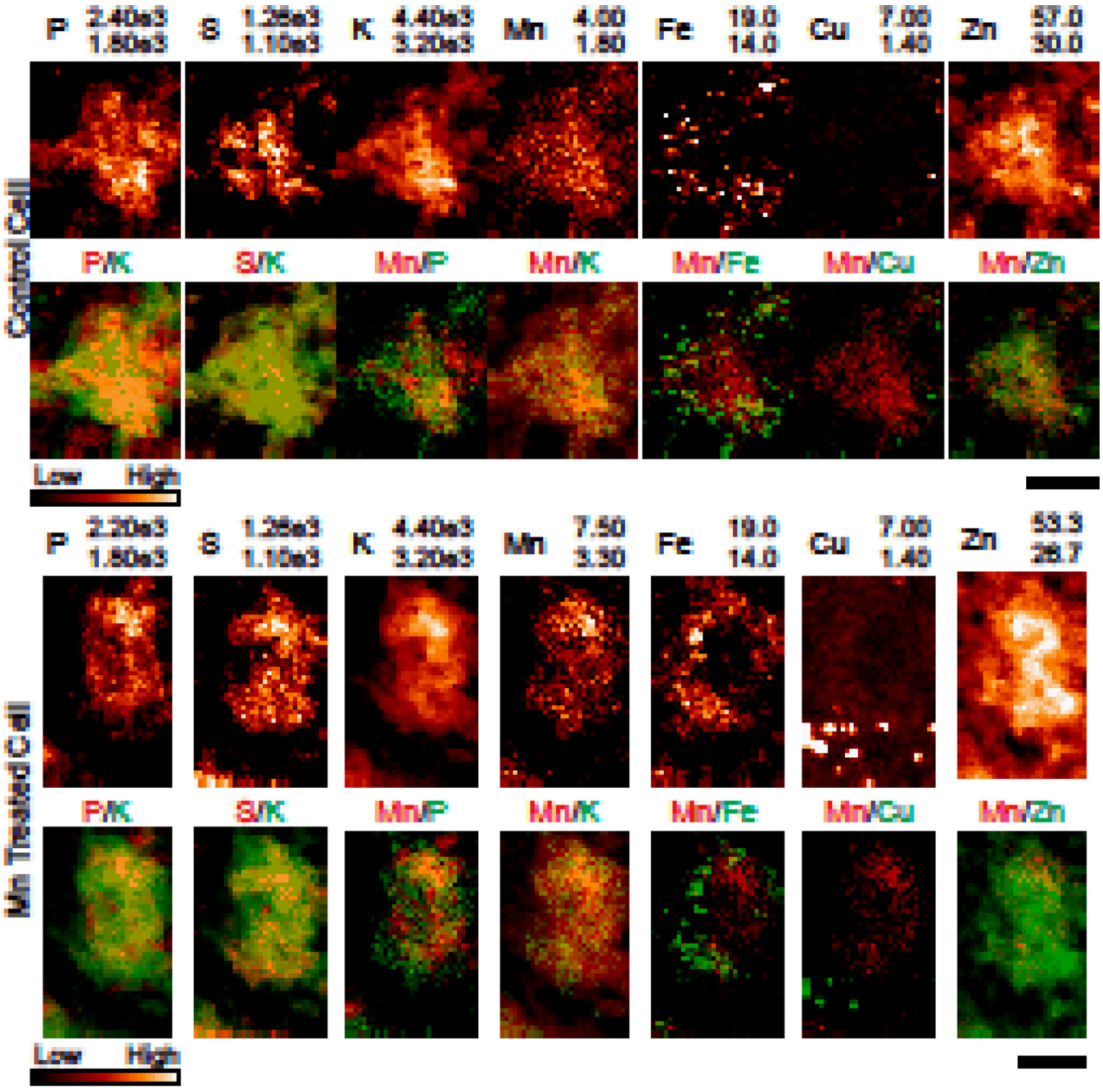

Fig. 4. XRF images of single cells of the CA3

Single cell XRF image from control (top) and Mn treated (bottom) samples [*n* = 4/3 animals (control/treated); *n* = 11/9 cells (control/treated]. Note that the Mn scale is adjusted between the control and treated samples. Potassium helps to identify the cell body. All numbers are given in μg/g. Scale bar represents a length of 7.5μm.

Table 1

XRF imaging parameters

Beamline	Beam size (μm × μm)	Pixel size (μm × μm)	Dwell (s)	Energy (keV)	Flux (photons/s)	Figure
APS Sector 18	7 × 5	40 × 40	0.8	10.0	1.8×10^{11}	1 & 2
		7 × 7	0.8	10.0		3
APS Sector 2-ID-D	0.3 × 0.3	15 × 15	0.25 – 0.5	10.0		SI 1B
		3 × 3	0.5–1.5	10.0		SI 1C
		0.3 × 0.3	1.5	10.0	4×10^{9}	4, SI 2 & 3

Table 2

Average metal concentrations for the HPCf

			Control (μg/g)				Treated (μg/g)			
Region	**Study**	**Method**	**Mn**	**Fe**	**Cu**	**Zn**	**Mn**	**Fe**	**Cu**	**Zn**
HPCf[a]	Here	XRF	0.39 ± 0.03	10.45 ± 0.99	1.41 ± 0.08	13.57 ± 0.97	1.00 ± 0.19**	9.28 ± 1.17	1.39 ± 0.14	12.01 ± 1.71
	[75]	AAS	0.38 ± 0.04	12.40 ± 3.44	1.91 ± 0.05		0.72 ± 0.10**	19.2 ± 0.88**	2.26 ± 0.23*	
	[76]	AAS	0.287 ± 0.002	13.55 ± 0.26	2.122 ± 0.120	16.83 ± 0.36				
	[77]	NAA[b]/XRF	0.57 ± 0.17	16.42 ± 3.89	4.56 ± 0.85		2.11 ± 0.44*	14.01 ± 0.78	4.11 ± 0.35	
	[78c]	NAA	0.21 ± 0.04	32.0 ± 9.0	4.19 ± 1.31	15.84 ± 2.78	1.10 ± 0.22**	26 ± 7	7.65 ± 0.74*	14.04 ± 1.87
	[79d]	NAA	0.213 ± 0.060				0.360 ± 0.167*			
HPCf 1[a]	Here	XRF	0.36 ± 0.03	8.75± 0.82	1.34 ± 0.06	12.01± 0.94	0.98 ± 0.18**	8.14 ± 1.09	1.34 ± 0.15	11.32 ± 1.59
HPCf 2[a]	Here	XRF	0.41 ± 0.02	12.43 ± 0.86	1.67 ± 0.05	10.33 ± 0.99	0.98 ± 0.08**	11.84 ± 1.14	1.74 ± 0.11	9.37 ± 0.70+
	Here (7×7 μm^2)	XRF					0.62 ± 0.11	8.63 ± 0.70	1.11 ± 0.15	6.88 ± 0.71
EC	[49]	XRF	2.0 ±0.9	30.2 ±7.5	3.5 ±0.7	17.3 ±2.9	3.0 ±2.7	23.5 ±4.0	3.9 ±0.4	17.3 ±1.7
HPCf 3[e]	Here	XRF	0.41 ± 0.05	9.97 ± 1.30	1.19 ± 0.16	20.27 ± 2.43	1.21 ± 0.22**	8.51 ± 1.02	1.14 ± 0.09	18.71 ± 2.56
CA3/DG	[49]	XRF	2.5 ±1.6	36.4 ±13.7	2.9 ±0.4	55.0 ±8.6	5.0 ±2.4	23.8 ±5.9	2.4 ±0.7	46.9 ±4.4
HPCf 4[e]	Here	XRF	0.42 ± 0.05	15.14 ± 1.99	1.31 ± 0.08	17.07 ± 3.38	1.26 ± 0.13**	11.01 ± 1.40**	1.27 ± 0.17	15.63 ± 1.19
	Here (7×7 μm^2)	XRF					0.72 ± 0.12	10.31 ± 0.94	0.81 ± 0.17	10.97 ± 1.69
HPCf 5[e]	Here	XRF	0.37 ± 0.03	9.75 ± 1.60	1.27 ± 0.25	27.51 ± 4.37	1.21 ± 0.08**	7.68 ± 1.20+	1.09 ± 0.09	23.45 ± 1.82
	Here (7×7 μm^2)	XRF					0.63 ± 0.10	6.36 ± 0.88	0.95 ± 0.34	16.81 ± 1.99

+ $p < 0.1$,

* $p < 0.5$,

** $p < 0.01$ as compared to control

[a] n = 2/4 animals (control/treated).

[b] NAA used to measure Mn content; XRF was used for Fe and Cu measurements.

[c] Treated rodents exposed to 20 mg Mn/mL drinking water from birth to 120 days.

[d] Treated rodent exposed to 1 mg Mn/mL drinking water from birth to 130 days.

[e] $n = 2/3$ animals (control/treated).

Table 3

Linear fit parameters for HPCf regions

Fit parameters for scatter plots displayed in Fig. 2B (mean ± std). Fits are based on n = 10/22 points (control/treated).

		Slope	Intercept	Pearson	
				R	***p***
Mn/Fe	C	80.49 ± 85.26	−20.72 ± 32.44	0.87	<0.01
	T	−15.62 ± 6.62	27.02 ± 7.44	−0.33	0.14
Mn/Cu	C	13.41 ± 22.56	−3.86 ± 8.57	0.39	0.27
	T	−1.43 ± 0.68	2.89 ± 0.78	−0.52	0.01
Mn/Zn	C	−8.94 ± 51.32	19.42 ±19.29	−0.06	0.87
	T	45.23 ± 16.16	−34.62 ±17.99	0.68	<0.01

Table 4

Linear fit parameters for DG crest (mean ± std)

		Slope	Int.	Pearson		ANCOVA	
	Region	**μg/gmetal:μg/gMn**	**μg/g**	**r**	**p**	**F**	**p**
Fe/Mn	HPCf2	0.79 ± 0.11	8.14 ± 0.07	0.13	<0.01	92.24[a]	<0.01
	HPCf4	2.81 ± 0.17	8.29 ± 0.13	0.35	<0.01		
	HPCf5	−0.24 ± 0.19	6.51 ± 0.12	−0.03	0.20		
Cu/Mn	HPCf2	−0.28 ± 0.02	1.29 ± 0.01	−0.21	<0.01	13.47[b]	<0.01
	HPCf4	−0.01 ± 0.03	0.82 ± 0.02	−0.01	0.77		
	HPCf5	−0.06 ± 0.07	0.98 ± 0.05	−0.02	0.41		
Zn/Mn	HPCf2	3.22 ± 0.10	4.88 ± 0.06	0.51	<0.01	112.77[a]	<0.01
	HPCf4	−2.12 ± 0.33	12.48 ± 0.24	−0.15	<0.01		
	HPCf5	−0.12 ± 0.42	16.89 ± 0.27	−0.01	0.77		

[a] All slopes statistically different from each other

[b] Slope of this region is statistically different than the slopes of the other regions

Table 5

Average metal concentrations in HPCf CA3 cells

All values are reported in μg/g (mean ± std); *n* = 11/9 cells (control/treated) from *n* = 4/3 animals (control/treated). Three cells from each group were taken on 10μm thick sections.

	P (× 10^3)	K (× 10^3)	Mn	Fe	Cu	Zn
Control	1.79 ± 0.28	3.95 ± 0.50	2.31 ± 0.80	17.35 ± 5.24	2.34 ± 0.39	56.01 ± 18.36
Treated	1.68 ± 0.19	3.88 ± 0.14	5.62 ± 0.44*	15.17 ± 2.17	2.47 ± 0.63	50.29 ± 8.55

* $p < 0.05$ as compared to control.

Table 6

CA3 cell linear fit parameters

Stronger correlations are K/M and to a lesser extend Zn/Mn (mean ± std); *n* = 11/9 cells (control/treated) from *n* = 4/3 animals (control/treated). Three cells from each group were taken on 10μm thick sections.

		Slope	Pearson		ANCOVA	
		$\mu g/g_{metal}$:$\mu g/g_{Mn}$	*R*	*p*	*F*	*p*
Mn/P	C	109.5 ± 2.9	0.32	<0.01	586	<0.01
	T	34.8 ± 1.40	0.21	<0.01		
Mn/K	C	345.4 ± 4.4	0.57	<0.01	1675	<0.01
	T	149.0 ± 2.2	0.50	<0.01		
Mn/Fe	C	1.56 ± 0.09	0.15	<0.01	187	<0.01
	T	0.43 ± 0.02	0.15	<0.01		
Mn/Cu	C	0.07 ± 0.03	0.02	0.02	0.23	0.29
	T	0.03 ± 0.06	0.00	0.66		
Mn/Zn	C	5.05 ± 0.11	0.38	<0.01	687	<0.01
	T	2.05 ±0.05	0.33	<0.01		

Metallomics. Author manuscript; available in PMC 2014 November 01.